

# Impact of electronic correlations on the superconductivity of high-pressure CeH<sub>9</sub>

Siyu Chen<sup>1,2,\*</sup>, Yao Wei<sup>3</sup>, Bartomeu Monserrat<sup>2</sup>, Jan M. Tomczak<sup>3,4,\*</sup>, and Samuel Poncé<sup>5,6,\*</sup>

<sup>1</sup>TCM Group, Cavendish Laboratory, University of Cambridge, J. J. Thomson Avenue, Cambridge CB3 0HE, United Kingdom

<sup>2</sup>Department of Materials Science and Metallurgy, University of Cambridge, 27 Charles Babbage Road, Cambridge CB3 0FS, United Kingdom

<sup>3</sup>Department of Physics, King's College London, Strand, London WC2R 2LS, United Kingdom

<sup>4</sup>Institute of Solid State Physics, TU Wien, 1040 Vienna, Austria

<sup>5</sup>European Theoretical Spectroscopy Facility, Institute of Condensed Matter and Nanosciences, Université catholique de Louvain, Chemin des Étoiles 8, B-1348 Louvain-la-Neuve, Belgium

<sup>6</sup>WEL Research Institute, avenue Pasteur 6, 1300 Wavre, Belgium

\*e-mails: sc2090@cam.ac.uk, jan.tomczak@kcl.ac.uk, samuel.pon@gmail.com

## ABSTRACT

Rare-earth superhydrides have attracted considerable attention because of their high critical superconducting temperature under extreme pressures. They are known to have localized valence electrons, implying strong electronic correlations. However, such many-body effects are rarely included in first-principles studies of rare-earth superhydrides because of the complexity of their high-pressure phases. In this work, we use a combined density functional theory and dynamical mean-field theory approach to study both electrons and phonons in the prototypical rare-earth superhydride CeH<sub>9</sub>, shedding light on the impact of electronic correlations on its critical temperature for phonon-mediated superconductivity. Our findings indicate that electronic correlations result in a larger electronic density at the Fermi level, a bigger superconducting gap, and softer vibrational modes associated with hydrogen atoms. Together, the inclusion of these correlation signatures increases the Migdal-Eliashberg superconducting critical temperature from 47 K to 96 K, close to the measured 95 K. Our results reconcile experimental observations and theoretical predictions for CeH<sub>9</sub> and herald a path towards the quantitative modeling of phonon-mediated superconductivity for interacting electron systems.

## Introduction

Pressure-induced metallic hydrogen stands as the holy grail of high-pressure physics, with a long belief in its potential room-temperature superconductivity [1]. Although the theoretical pathway is well-established, the experimental realization of metallic hydrogen is hindered by the ultra-high pressure required for metallization and the difficulty of probing samples under extreme conditions. A significant advancement in this field came with Ashcroft's proposal of *chemical pre-compression* [2, 3]. This scheme widens the phase space in which a high-temperature superconductor can be found, ultimately leading to superhydrides that transition to a superconducting state at pressures lower than those predicted for elemental hydrogen [4].

Among the various candidates, rare-earth metal superhydrides have shown great promise, especially with the discovery of LaH<sub>10</sub> [5–8]. It exhibits a superconducting critical temperature of around 250 K at 170 GPa, marking the highest measured superconducting critical temperature to date. Furthermore, cerium superhydrides (CeH<sub>*n*</sub> with *n* = 9 or 10) have also attracted attention: although their maximum superconducting critical temperatures do not exceed that of

LaH<sub>10</sub>, they reach a relatively high superconducting critical temperature (around 100 K) at pressures on the order of 100 GPa or less [9–11]. This lower-pressure regime not only simplifies high-pressure synthesis and characterization but also further brings the goal of ambient-pressure superconductivity closer to fruition. In general, numerous rare-earth superhydrides have been predicted and synthesized in the past decade [5, 9, 12–20], but a pivotal yet unresolved question persists. What role do electronic correlations, induced by the *f*-electrons of the rare-earth elements, play in these high-pressure compounds? In LaH<sub>10</sub>, it has been observed that external pressure destabilizes the 6*s*- and 5*d*-orbitals of La, making the 4*f*-orbitals energetically more favorable [21]. As a result, the electronic states of LaH<sub>10</sub> near the Fermi level are composed of La 4*f*- and H 1*s*-orbitals [22]. We note that these states involving La 4*f*-orbitals are strongly localized and generally cannot be well described by density functional theory (DFT) [23, 24].

To gain insight into the question of the role of electronic correlation in rare-earth superhydride, we choose CeH<sub>9</sub> as a representative example and explore many-body effects using a combination method of DFT and dynamical mean field

theory (DMFT), known as DFT+DMFT [25–33]. Previous studies have shown that the strong correlation nature of cerium  $f$ -electrons plays a pivotal role in the isostructural phase transition of cerium in its elemental form [34–38], in cerium intermetallic compounds [39, 40], other rare-earth metals [41, 42], Kondo insulators [43, 44], as well as heavy-fermion systems [45, 46]. We address the notable gap between the experimental results [9–11, 14] and theoretical forecasts [12, 13, 47] regarding the critical temperature of phonon-mediated superconductivity in CeH<sub>9</sub> under high pressure. Theoretical calculations based on DFT underestimate the superconducting critical temperature by nearly 50% [9], prompting speculation about the role of electronic correlations. Our work enhances the description of phonon-mediated superconductivity by incorporating electron-correlation effects for electronic and phononic interactions.

## Results and discussion

### Correlated electrons

We study the impact of electronic correlation effects in CeH<sub>9</sub> by comparing DFT band-theory results to DMFT many-body calculations. To this end, we first obtain the crystal structure of CeH<sub>9</sub> from first principles by optimizing the internal atomic coordinates and the lattice constants of the crystal under 200 GPa using DFT, see Sec. S1 in the Supplementary Information (SI). We find that including the Ce 4*f*-electron as valence electrons in the pseudopotential calculations is necessary to obtain lattice parameters in agreement with measurements [48], suggesting that the Ce-4*f*-electrons, although being more closely bound, are not atomic-like. Turning to the electronic structure, we compare in Fig. 1 the DFT band-structure (red lines) to the DMFT spectral function (color map). As in LaH<sub>10</sub> [22], the dispersions around the Fermi level are dominated by H 1*s*-orbitals that hybridize considerably with the Ce 4*f*-orbitals, see Sec. S2 of the SI for additional details. Upon examining the intersections of the (red) bands and the high-intensity spectral features with the Fermi level ( $\omega = 0$ ; horizontal white line), we observe that the incorporation of electronic correlation effects results in a Fermi surface that remains largely unaltered in comparison to DFT calculations. In addition, the multiple electron and hole pockets remain qualitatively similar throughout the Brillouin zone. Quantitatively, however, higher-energy states are notably renormalized towards the Fermi level. For example, the electron pocket at the  $\Gamma$  point becomes 0.4 eV shallower as compared to the DFT result. Notable are the energy shifts of the nondispersive Ce 4*f*-orbital bands, originally 1 to 2 eV above the Fermi level, which decrease significantly in DFT + DMFT computations.

By comparing the DFT+DMFT density of state (DOS) with the DFT one in Fig. 2a, we see that the inclusion of electronic correlations shifts the prominent Ce 4*f*-dominated spectral features down by at least 0.5 eV. Since the 4*f*-states are localized, their lowering causes the total spectral weight at the Fermi level to increase by 26%, as can be seen in the

inset of Fig. 2a.

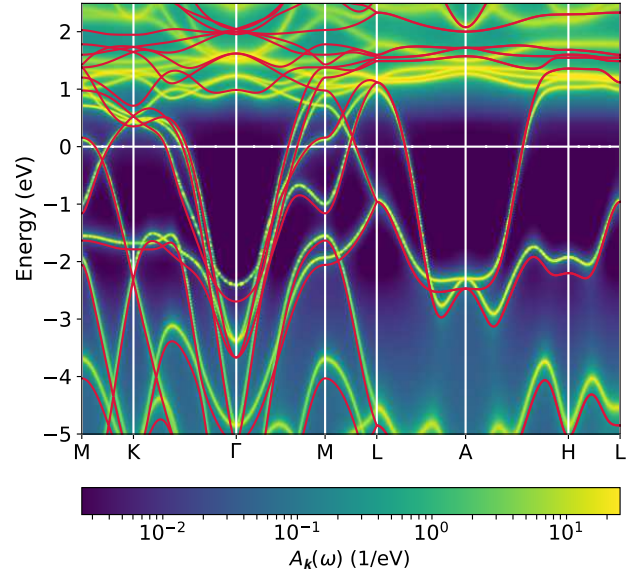


**Fig. 1. | Comparison of the electronic bands obtained from DFT and spectral function from DMFT.**

Momentum-resolved spectral function  $A_{\mathbf{k}}(\omega)$  of CeH<sub>9</sub> along a high-symmetry path calculated with DMFT (color map) compared to the energy bands calculated by DFT (solid red lines).

Dynamical correlations drive these spectral changes: DFT + U produces a DOS similar to DFT, see Fig. S5 of SI. Meanwhile, the orbital occupation of Ce 4*f* increases slightly from 1.42 in DFT to 1.58 with DFT+DMFT. This charge transfer results in effective hole-doping of the H 1*s*-spectral weight. Wang *et al.* [47] noted that chemical hole doping can shift the electron pocket at  $\Gamma$  toward the Fermi level, enhancing the electron-phonon coupling. Remarkably, electronic correlations cause a similar effect in the stoichiometric compound. However, despite broadenings in DFT+DMFT, the excitation spectrum remains coherent and band-like. This can be understood by examining the DFT+DMFT self-energy  $\Sigma(\omega)$ , from which we derive an averaged local quasiparticle weight  $Z = (1 - d\text{Re}\Sigma(\omega)/d\omega)^{-1} = 0.8$ . The imaginary part of the self-energy is negligible near  $\pm 3$  eV of the Fermi level, allowing a quasiparticle description of the low-energy spectrum. See the Method Section and SI Sec. S3 for more details.

### Phonons in the presence of correlated electrons

We now investigate the impact of electronic correlations on the phonon modes. We compute phonon dispersion via the finite difference method [49, 50], at the DFT level using the forces arising from small atomic displacements and at the DFT+DMFT level using forces which are instead defined from the derivatives of the free energy  $F = E - TS$ , where  $T$  is the electronic temperature and  $S$  is the impurity entropy [32]. These calculations are enabled by the efficient methodology in Ref. [51]. Figure 2(b) compares the phonon DOS

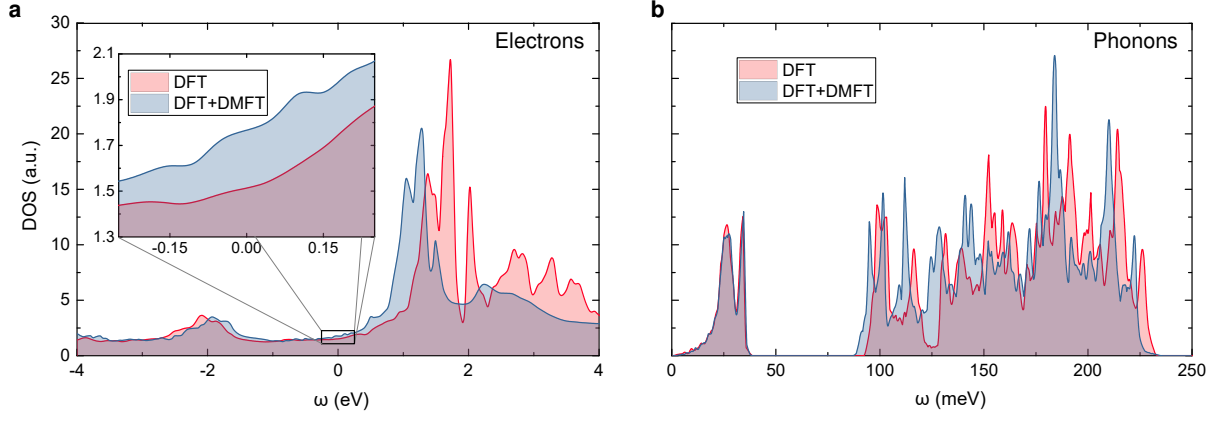


**Fig. 2. | Comparison of density of states (DOS) obtained from DFT and DMFT. a** Electronic and **b** phononic DOS of CeH<sub>9</sub> calculated with DFT and DFT+DMFT, respectively. The inset in **a** highlights the increase in the DOS near the Fermi level.

of CeH<sub>9</sub> obtained within DFT and DFT + DMFT. Because of the significant difference in the atomic masses, the vibrations of cerium and hydrogen are largely decoupled, resulting in a clear energy separation in the phonon DOS. The low-frequency modes ( $\omega < 50$  meV) arise predominantly from cerium vibrations, while the high-frequency (optical) modes ( $\omega > 50$  meV) emerge from dynamical distortions of the hydrogen cages. The highest frequency reaches 240 meV at the DFT level (red curve), slightly lower than in LaH<sub>10</sub> in which the hardest mode reaches approximately 275 meV under similar pressure conditions [52]. The effect of DMFT is to soften hydrogen vibrations.

Given that the same structure is used in both approaches, we exclude a phonon softening through volume expansion and attribute it to electronic correlations captured by DMFT. This can be explained by the more localized nature of DMFT electrons, which have weaker chemical bonds, and is also observed in the iron-based superconductor with inelastic neutron scattering [53].

### Superconductivity

Finally, we examine the influence of electronic correlations on the superconductivity of CeH<sub>9</sub>. To contextualize our results, it is worth first clarifying the hierarchy of methods used to evaluate  $T_c$ : (i) the McMillan-Allen-Dynes (AD) formula ( $T_c^{\text{AD}}$ ) [54, 55], which provides a closed-form expression for  $T_c$  as follows

$$T_c^{\text{AD}} = \frac{\omega_{\text{ln}}}{1.2k_B} \exp \left[ \frac{-1.04(1+\lambda)}{\lambda - \mu_c(1+0.62\lambda)} \right], \quad (1)$$

where  $\omega_{\text{ln}}$  is the logarithmic averaged phonon frequency,  $k_B$  denotes the Boltzmann constant,  $\lambda$  is the el-ph coupling strength, and  $\mu_c$  is the Morel-Anderson pseudopotential accounting for Coulomb repulsion of the system [56]; (ii) the isotropic ( $T_c^{\text{iso}}$ ) and (iii) anisotropic Eliashberg equations ( $T_c^{\text{aniso}}$ ) [57, 58], in which  $T_c$  is determined implicitly by identifying the highest temperature at which a nonzero superconducting gap  $\Delta$  appears. These three methods provide a

progressively more refined description of phonon-mediated superconductivity with increasing accuracy and computational cost.

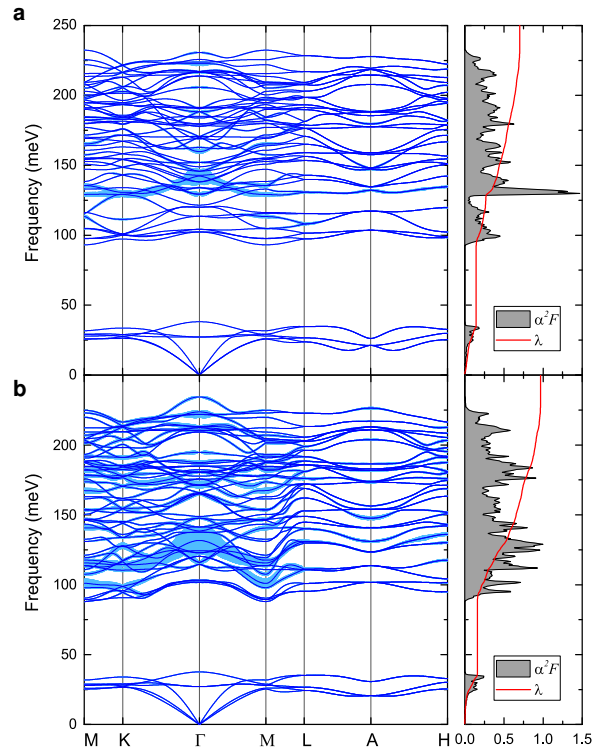


**Fig. 3. | Phonon and electron-phonon properties obtained from DFT and DMFT. Phonon dispersion, Eliashberg spectral function  $\alpha^2F(\omega)$ , and integrated electron-phonon coupling strength  $\lambda(\omega)$  as a function of phonon frequency  $\omega$  as calculated with **a** DFT and **b** DFT+DMFT. The linewidth of the phonon dispersion is proportional to  $\lambda(\omega)$  projected onto the phonon modes.**

We note that Plekhanov *et al.* [59] have used the AD formula to obtain a correlation-induced enhancement in  $T_c$ ,

with the many-body correction introduced directly at the level of the Eliashberg spectral function  $\alpha^2 F(\omega)$ . They obtain a  $T_c^{\text{AD}} = 150$  K at 200 GPa, which overestimates the experimental value of 95 K [9]. This overestimation may be attributed to the use of the atomic Hubbard-I [60] solver for the DMFT impurity model and the use of DFT phonons. Our approach overcomes these limitations through the use of the continuous-time quantum Monte Carlo solver [37, 61] which is unbiased towards electron localization, and by ensuring an equal-footing treatment of DMFT electrons and phonons.

Interestingly, with both electrons and phonons described at the DFT level, we find that the el-ph coupling strength for CeH<sub>9</sub> is  $\lambda = 2 \int_0^\infty d\omega \alpha^2 F(\omega)/\omega = 0.70$ . We then compute the superconducting critical temperatures from the AD formula finding  $T_c^{\text{AD}} \simeq 30$  K, and by solving the isotropic and anisotropic Eliashberg equations, leading to  $T_c^{\text{iso}} \simeq 37$  K and  $T_c^{\text{aniso}} \simeq 47$  K, respectively. As anticipated, the McMillan–Allen–Dynes estimate is the lowest, since that formula is formally valid only for low- $T_c$  superconductors. Our values for  $\lambda$ ,  $T_c^{\text{AD}}$  and  $T_c^{\text{iso}}$  agree well with a previous study [9]. The Eliashberg treatment improves the prediction but the *anisotropic* Eliashberg solution demonstrates that anisotropy significantly increases the predicted  $T_c$ , bringing it closer to experimental observations.

Figure 3a shows the integrated el-ph coupling strength,  $\lambda(\omega) = 2 \int_0^\omega d\omega' \alpha^2 F(\omega')/\omega$ , projected onto the phonon dispersion along with the Eliashberg function  $\alpha^2 F(\omega)$ . We find that  $\lambda(\omega)$  is distributed in a nonuniform manner among the phonon modes and the phonon Brillouin zone, with approximately 80% of the total el-ph coupling strength arising from the optical phonon modes of hydrogen and the remaining 20% from the phonon modes of cerium. In particular, as highlighted by the linewidth in Fig. 3a, phonon modes with frequency around 125 meV are highly coupled to electrons, leading to a significant peak in the Eliashberg function  $\alpha^2 F(\omega)$ . This frequency range is also where we observed a significant softening of the hydrogen mode by electronic correlations.

To go further, we substitute the electron Hamiltonian and phonon dynamical matrices obtained at the DFT level with their counterparts at the DMFT level. These two substitutions will affect the electronic dispersion, the phonon dispersion, and, in principle, the el-ph coupling matrix elements. In this work, we neglect the effect of the latter and use DFT el-ph matrix elements throughout. Current implementations of the Migdal-Eliashberg theory of superconductivity are based on the quasiparticle approximation. Therefore, we construct from our DFT+DMFT calculations an effective quasiparticle band structure for CeH<sub>9</sub>. The construction of a renormalized band-structure is possible as the real-part of the self-energy can, to good approximation, be linearized around the Fermi level, while its imaginary part is small. Then, an effective band structure can be found as the solutions  $E_{n\mathbf{k}}$  of the linearized quasiparticle equation [63]

$$\det(E_{n\mathbf{k}}\mathbb{1} - \mathbf{Z}_{\mathbf{k}} [\mathbf{H}_{\mathbf{k}}^{\text{DFT+DMFT}} + \Re\{\mathbf{\Sigma}_{\mathbf{k}}(0)\} - \mu\mathbb{1}]) = 0, \quad (2)$$

which is written in the band basis. Bold quantities are matrices in the band indices  $n$ ,  $\mathbb{1}$  is the identity matrix,  $\mathbf{Z}_{\mathbf{k}} = (1 - d\Re\{\mathbf{\Sigma}_{\mathbf{k}}(\omega)/d\omega|_{\omega=0})^{-1}$  is the quasiparticle weight which approaches unity in a noninteracting system and zero in the limit of extremely strong correlations,  $\mathbf{H}_{\mathbf{k}}^{\text{DFT+DMFT}} = \text{diag}(\dots, \epsilon_{n\mathbf{k}}, \dots)$  the Kohn-Sham Hamiltonian at the DFT+DMFT self-consistent charge density, and  $\mu$  is the chemical potential.

	$T_c^{\text{aniso}}$ (K)	$T_c^{\text{iso}}$ (K)	$T_c^{\text{AD}}$ (K)	$P$ (GPa)	$\lambda$	$\omega_{\text{in}}$ (meV)
This work						
el <sup>DFT</sup> + ph <sup>DFT</sup>	47	37	30	200	0.70	96
el <sup>DFT</sup> + ph <sup>DMFT</sup>	53	43	35	200	0.71	108
el <sup>DMFT</sup> + ph <sup>DFT</sup>	87	77	59	200	0.95	93
el <sup>DMFT</sup> + ph <sup>DMFT</sup>	96	86	69	200	0.97	106
Prior works						
el <sup>DFT</sup> + ph <sup>DFT</sup> [12]	-	50	-	100	0.9	-
el <sup>DFT</sup> + ph <sup>DFT</sup> [47]	-	74	-	100	1.04	-
el <sup>DFT</sup> + ph <sup>DFT</sup> [9]	-	49	42	150	0.85	93
el <sup>DFT</sup> + ph <sup>DFT</sup> [9]	-	31	26	200	0.68	109
el <sup>DFT</sup> + ph <sup>DFT</sup> [13]	-	-	74	250	0.97	112
el <sup>DMFT</sup> + ph <sup>DFT</sup> [59]	-	-	150	200	1.06	154
experiment [9]		95		110	-	-
experiment [9]		95		150	-	-
experiment [10]		110		110	-	-
experiment [11]		90		116	-	-

**Table 1. Critical temperatures and superconducting parameters for CeH<sub>9</sub>.** We report the logarithmic averaged phonon frequency ( $\omega_{\text{in}}$ ) and electron-phonon coupling strength ( $\lambda$ ) entering the Allen-Dynes  $T_c^{\text{AD}}$ , isotropic Migdal-Eliashberg  $T_c^{\text{iso}}$ , and anisotropic Migdal-Eliashberg  $T_c^{\text{aniso}}$ . Our calculations describe the electron-phonon pairing on four levels of sophistication and are compared to previous theoretical works at the DFT level and experimental measurements. All theoretical values of  $T_c$  reported in the table are calculated with the Morel-Anderson pseudopotential  $\mu_c = 0.13$  except Ref. [9] which uses  $\mu_c = 0.15$ .

We validate the quality of the effective band structure obtained using the above quasiparticle approximation in Sec. S4 of the SI. Using this effective band structure and the DMFT phonon spectrum obtained previously, we calculate the el-ph coupling strength and the Eliashberg function at the DMFT level, as shown in Fig. 3b. The total coupling strength in this case is found to increase by nearly 39%, reaching  $\lambda \simeq 0.97$ . This increment supports a substantial elevation in the critical temperature, which increases from  $T_c^{\text{AD}} = 30$  K at the DFT level to  $T_c^{\text{AD}} = 69$  K at the DMFT level. We traced the increase in  $T_c$  to changes in specific regions in the Brillouin zone.

Figures 4a-b compare the superconducting gap  $\Delta$  on the Fermi surface of CeH<sub>9</sub> at 10 K. We find that in the case of DFT the superconducting gap is quite uniform across the Fermi surface, with an average magnitude of approximately 6.3 meV that varies by  $\pm 2.5$  meV through the Brillouin zone. In con-



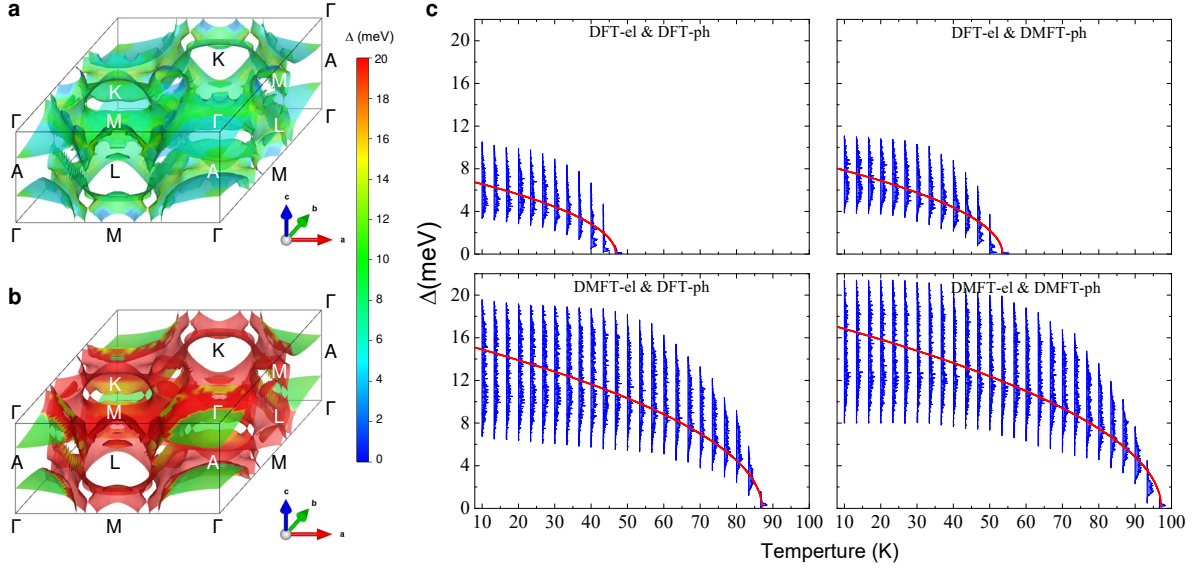


**Fig. 4. | Anisotropic superconducting gap of CeH<sub>9</sub>.** Calculated superconducting gap  $\Delta$  on the Fermi surface at 10 K computed with **a** DFT and **b** DFT+DMFT. **c** Anisotropic Migdal-Eliashberg superconducting gap  $\Delta$  as a function of temperature. We consider four cases: (top left) DFT electrons with DFT phonons, (bottom left) DMFT electrons with DFT phonons, (top right) DFT electrons with DMFT phonons, and (bottom right) DMFT electrons with DMFT phonons. The solid red line represents the temperature dependence of the superconducting gap expected from the BCS theory [62] in the weak-coupling limit where  $\Delta(T) = A\sqrt{1 - T/T_c}$ , where  $A$  is a fitting constant.

trast, at the DMFT level, the superconducting gap around the corner of the Brillouin zone (i.e. the  $K$  point) exhibits a remarkable increase, up to 20 meV, which explains the elevated superconducting critical temperature, from  $T_c^{\text{aniso}} = 47$  K at the DFT level to  $T_c^{\text{aniso}} = 96$  K at the DMFT level.

To gain further insights into the role of electronic correlation, we consider two ‘intermediate scenarios’ of el-ph coupling: DMFT electrons are paired with DFT phonons, and DFT electrons are paired with DMFT phonons. Figure 4c shows the energy distribution of the superconducting gap  $\Delta$  as a function of temperature for our previous results at the DFT and DMFT levels, as well as for the two intermediate scenarios. The superconducting gap is seen to close gradually with increasing temperature, vanishing at various critical values for each case. Table 1 summarizes the critical temperatures obtained, together with the corresponding superconducting parameters, offering a hierarchical comparison also with existing DFT studies and experimental measurements.

Our results align closely with previous studies for DFT but are underestimated by 50% measurements at comparable pressures. In contrast, our value at the DMFT level,  $T_c^{\text{aniso}} = 96$  K at 200 GPa, is in excellent agreement with the experimental value,  $T_c = 95$  K at the closest pressure of 150 GPa. Dissecting the influence of electronic correlations on the different ingredients entering the calculation of  $T_c$ , we find that the DMFT renormalization of the electronic structure is the main driving force behind the increased critical temperature. Indeed, keeping the phonons at the DFT-level, the effect of DMFT on electrons almost doubles the  $T_c$ . Indeed, as shown

in Fig 2a, the increased DOS at the Fermi level,  $D(E_F)$ , facilitates the formation of more Cooper pairs, leading to a higher superconducting critical temperature [62] for which  $T_c \propto \exp(1/VD(E_F))$  with  $V$  the average el-ph coupling constant. Finally, we also discover that exclusively renormalizing the electronic structure with DMFT still leads to a substantial underestimation of the superconducting critical temperature. It is necessary to also include the phonon-softening effect owing to electronic correlations to quantitatively reconcile the theoretical findings with the experimental data.

## Conclusion

In summary, we have used a combination of DFT and DMFT to study electrons and phonons of CeH<sub>9</sub> under high pressure, demonstrating that strong electronic correlations arising from cerium  $4f$ -states play an important role in this system. Many-body effects increase electron masses, produce a larger spectrum at the Fermi level, and soften hydrogen vibrational modes. Combining DFT+DMFT with the Migdal-Eliashberg theory of superconductivity, we were able to investigate the role of electronic correlations for the critical temperatures of phonon-mediated superconductivity in CeH<sub>9</sub>. Our findings indicate that the dominant correction to the critical temperature comes from the many-body renormalization of the electronic structure. However, we find that the renormalization of phonons is significant and cannot be neglected. The many-body-driven change in the critical superconducting temperature is 50 K. Future extensions of this work should address the impact of correlations on the el-ph coupling. In addition, pre-

vious works indicate that *non-local* exchange and correlation effects can increase the el-ph coupling [64, 65]. Overall, our findings shed new light on phonon-mediated high-temperature superconductivity in rare-earth superhydrides.

## Methods

We have performed DFT + DMFT calculations at inverse temperature  $\beta = 20 \text{ eV}^{-1}$  (i.e.  $T \simeq 580 \text{ K}$ ) with the embedded DMFT functional package EDMFT [32] integrated with the all-electron DFT code WIEN2K [66]. The DMFT impurity problem is solved using a continuous-time quantum Monte Carlo algorithm [37, 61]. We use the nominal double counting scheme [37], with an occupation fixed to 2, as the DFT-calculated valency of Ce under pressure is found to be 1.48 (greater than the nominal 1 electron) indicating an increased *f*-electron occupancy compared to the idealized trivalent state. A brief summary of Haule *et al.*'s implementation [32] is given in SI Sec. S5. We analytically continue the Matsubara self-energy to real frequencies using the maximum entropy method [67]. The quasiparticle weight was extracted from both Matsubara and real-frequency data and was found to be consistent. We have cross-checked the WIEN2K all-electron results with the pseudopotential-based DFT packages CASTEP [68, 69] and QUANTUM ESPRESSO [70, 71] that were used previously in Ref. [59], using the same ultrasoft pseudopotentials that CASTEP generates on the fly for both codes. The valence electron configurations of  $5s^2 5p^6 4f^1 5d^1 6s^2$  (with *4f*-electrons explicitly included) and  $1s$  are adopted for the Ce and H atoms, respectively. Figure S9 in SI Sec. S6 shows a favorable comparison. Convergence tests at the DFT level yielded an energy cut-off of 800 eV for CASTEP and for QUANTUM ESPRESSO. For WIEN2K, convergence is achieved when the product of the smallest atomic-sphere radius and the maximum reciprocal-space vector in the plane-wave expansion reaches 7. A  $\Gamma$ -centered **k**-point grid of size  $12 \times 12 \times 6$  is used for all three packages. The exchange-correlation functional is approximated using PBE [72]. As was done in previous works [9, 12, 13, 47, 59], we omit spin-orbit coupling for technical reasons. In the DFT + DMFT calculations, we use an on-site Coulomb interaction (Hubbard *U*) of  $U = 6.0 \text{ eV}$  and a Hund's coupling  $J = 0.7 \text{ eV}$  for the cerium *f* orbitals. This choice is comparable to previous values that were successfully used for elemental cerium [35–38], CeH<sub>9</sub> [59], and other Ce-compounds [44]. Note that we neglect any potential impact of pressure on Hubbard *U* [41, 73]. We also omit any additional renormalizations of the DMFT electronic structure that arise from the electron-phonon coupling [74, 75].

For the lattice dynamics calculations, we use finite difference with an in-house code which offers a versatile interface with DFT and DFT+DMFT [51], to calculate the phonon spectrum of CeH<sub>9</sub>. Considering that the computational cost of DFT+DMFT exhibits a particularly unfavorable scaling with the system size, we employ the non-diagonal supercell technique [76] to sample a  $2 \times 2 \times 2$  **q**-point grid in the Brillouin

zone and then interpolate the result to obtain dynamical matrices on a **q**-point grid of  $6 \times 6 \times 3$ . Specifically, we use four different supercells constructed with the following supercell matrices:  $\begin{pmatrix} 1 & 0 & 0 \\ 0 & 1 & 0 \\ 0 & 0 & 1 \end{pmatrix}$ ,  $\begin{pmatrix} 1 & 0 & 0 \\ 0 & 1 & 0 \\ 0 & 0 & 2 \end{pmatrix}$ ,  $\begin{pmatrix} 1 & 0 & 0 \\ 0 & 2 & 0 \\ 0 & 0 & 1 \end{pmatrix}$ , and  $\begin{pmatrix} 1 & 0 & 0 \\ 0 & 1 & -1 \\ 1 & 2 & 0 \end{pmatrix}$ , the first one provides access to  $\Gamma$  – **q**-point, then the second one provides access to the  $(0, 0, 1/2)$  **q**-point, the third one to the  $(0, 1/2, 0)$  **q**-point, and the forth one to the  $(1/2, 1/2, 1/2)$  **q**-point. All other **q**-points on the  $2 \times 2 \times 2$  grid are related to these four by symmetry and therefore explicit calculations are not necessary.

To evaluate the superconducting critical temperature  $T_c$ , we used EPW [77, 78] to interpolate the el-ph coupling matrix calculated with the density functional perturbation theory as implemented in QUANTUM ESPRESSO from a  $12 \times 12 \times 6$  **k**-point grid and a  $6 \times 6 \times 3$  **q**-point grid to a  $48 \times 48 \times 24$  **k**-point grid and a  $24 \times 24 \times 12$  **q**-point grid. In particular, for  $T_c$  calculations at the DFT+DMFT level, the electronic and phononic degrees of freedom obtained from standard DFT are replaced with the counterparts obtained from DFT+DMFT. We used a standard value for the Morel-Anderson pseudopotential  $\mu_c = 0.13$  which accounts for Coulomb repulsion of the system [56] in all our calculations. We present the Eliashberg theory of superconductivity as implemented in EPW in SI Sec. S7.

## Data availability

The data that support the findings of this study are available in the Supplementary Information and on the Materials Cloud Archive.

## Code availability

The WIEN2K code used in this study is a commercial software, available from <http://susi.theochem.tuwien.ac.at>. The QUANTUM ESPRESSO code used in this research is open source: <https://www.quantum-espresso.org>. The CASTEP code used in this study is freely available at <https://www.castep.org> for academic research. The EPW code used in this research is open source: <https://epw-code.org>. The ana\_cont code used in this study is open source: [https://github.com/josefkaufmann/ana\\_cont](https://github.com/josefkaufmann/ana_cont).

## Authors contributions

S.C. and Y.W. contributed equally to this work. S.C. performed the DMFT spectral function and superconducting calculations, while Y.W. performed the DMFT phonon calculations. S.P. and J.M.T provided technical help with the WIEN2K and EPW software. S.P., B.M. and J.M.T supervised the work. All authors reviewed and approved the final version of the manuscript.

## Competing interests

The authors declare no competing interests.

## References

1. Ashcroft, N. W. Metallic hydrogen: A high-temperature superconductor? *Phys. Rev. Lett.* **21**, 1748–1749, DOI: [10.1103/PhysRevLett.21.1748](https://doi.org/10.1103/PhysRevLett.21.1748) (1968).
2. Ashcroft, N. W. Hydrogen dominant metallic alloys: High temperature superconductors? *Phys. Rev. Lett.* **92**, 187002, DOI: [10.1103/PhysRevLett.92.187002](https://doi.org/10.1103/PhysRevLett.92.187002) (2004).
3. Ashcroft, N. W. Bridgman's high-pressure atomic destructibility and its growing legacy of ordered states. *J. Phys.: Condens. Matter* **16**, S945, DOI: [10.1088/0953-8984/16/14/003](https://doi.org/10.1088/0953-8984/16/14/003) (2004).
4. Boeri, L. *et al.* The 2021 room-temperature superconductivity roadmap. *J. Phys.: Cond. Matter* **34**, 183002, DOI: [10.1088/1361-648X/ac2864](https://doi.org/10.1088/1361-648X/ac2864) (2022).
5. Drozdov, A. P. *et al.* Superconductivity at 250 K in lanthanum hydride under high pressures. *Nature* **569**, 528–531, DOI: [10.1038/s41586-019-1201-8](https://doi.org/10.1038/s41586-019-1201-8) (2019).
6. Somayazulu, M. *et al.* Evidence for Superconductivity above 260 K in Lanthanum Superhydride at Megabar Pressures. *Phys. Rev. Lett.* **122**, 027001, DOI: [10.1103/PhysRevLett.122.027001](https://doi.org/10.1103/PhysRevLett.122.027001) (2019).
7. Hong, F. *et al.* Superconductivity of Lanthanum Superhydride Investigated Using the Standard Four-Probe Configuration under High Pressures. *Chin. Phys. Lett.* **37**, 107401, DOI: [10.1088/0256-307X/37/10/107401](https://doi.org/10.1088/0256-307X/37/10/107401) (2020).
8. Sun, D. *et al.* High-temperature superconductivity on the verge of a structural instability in lanthanum superhydride. *Nat. Commun.* **12**, 6863, DOI: [10.1038/s41467-021-26706-w](https://doi.org/10.1038/s41467-021-26706-w) (2021).
9. Chen, W. *et al.* High-temperature superconducting phases in cerium superhydride with a  $T_c$  up to 115 K below a pressure of 1 megabar. *Phys. Rev. Lett.* **127**, 117001, DOI: [10.1103/PhysRevLett.127.117001](https://doi.org/10.1103/PhysRevLett.127.117001) (2021).
10. Cao, Z.-Y. *et al.* Probing superconducting gap in CeH<sub>9</sub> under pressure. *arXiv preprint arXiv:2401.12682* DOI: [10.48550/arXiv.2401.12682](https://doi.org/10.48550/arXiv.2401.12682) (2024).
11. Semenok, D. *et al.* Evidence for pseudogap phase in cerium superhydrides: CeH<sub>10</sub> and CeH<sub>9</sub>. *arXiv preprint arXiv:2307.11742* DOI: [10.48550/arXiv.2307.11742](https://doi.org/10.48550/arXiv.2307.11742) (2023).
12. Peng, F. *et al.* Hydrogen clathrate structures in rare earth hydrides at high pressures: Possible route to room-temperature superconductivity. *Phys. Rev. Lett.* **119**, 107001, DOI: [10.1103/PhysRevLett.119.107001](https://doi.org/10.1103/PhysRevLett.119.107001) (2017).
13. Sun, W., Kuang, X., Keen, H. D. J., Lu, C. & Hermann, A. Second group of high-pressure high-temperature lanthanide polyhydride superconductors. *Phys. Rev. B* **102**, 144524, DOI: [10.1103/PhysRevB.102.144524](https://doi.org/10.1103/PhysRevB.102.144524) (2020).
14. Guo, J., Chen, S., Chen, W., Huang, X. & Cui, T. Advances in the synthesis and superconductivity of lanthanide polyhydrides under high pressure. *Front. electr. mater.* **2**, 906213, DOI: [10.3389/femat.2022.906213](https://doi.org/10.3389/femat.2022.906213) (2022).
15. Zhong, X. *et al.* Prediction of above-room-temperature superconductivity in lanthanide/actinide extreme superhydrides. *J. Am. Chem. Soc.* **144**, 13394–13400, DOI: [10.1021/jacs.2c05834](https://doi.org/10.1021/jacs.2c05834) (2022).
16. Zhou, D. *et al.* Superconducting praseodymium superhydrides. *Sci. Adv.* **6**, eaax6849, DOI: [10.1126/sciadv.aax6849](https://doi.org/10.1126/sciadv.aax6849) (2020).
17. Zhou, D. *et al.* High-pressure synthesis of magnetic neodymium polyhydrides. *J. Am. Chem. Soc.* **142**, 2803–2811, DOI: [10.1021/jacs.9b10439](https://doi.org/10.1021/jacs.9b10439) (2020).
18. Kong, P. *et al.* Superconductivity up to 243 K in the yttrium-hydrogen system under high pressure. *Nat. Commun.* **12**, 5075, DOI: [10.1038/s41467-021-25372-2](https://doi.org/10.1038/s41467-021-25372-2) (2021).
19. Shao, M. *et al.* Superconducting ScH<sub>3</sub> and LuH<sub>3</sub> at megabar pressures. *Inorg. Chem.* **60**, 15330–15335, DOI: [10.1021/acs.inorgchem.1c01960](https://doi.org/10.1021/acs.inorgchem.1c01960) (2021).
20. Troyan, I. A. *et al.* Anomalous high-temperature superconductivity in YH<sub>6</sub>. *Adv. Mater.* **33**, 2006832, DOI: <https://doi.org/10.1002/adma.202006832> (2021).
21. Liu, H., Naumov, I. I., Hoffmann, R., Ashcroft, N. W. & Hemley, R. J. Potential high- $T_c$  superconducting lanthanum and yttrium hydrides at high pressure. *Proc. Natl. Acad. Sci.* **114**, 6990–6995, DOI: [10.1073/pnas.1704505114](https://doi.org/10.1073/pnas.1704505114) (2017).
22. Liu, L. *et al.* Microscopic mechanism of room-temperature superconductivity in compressed LaH<sub>10</sub>. *Phys. Rev. B* **99**, 140501, DOI: [10.1103/PhysRevB.99.140501](https://doi.org/10.1103/PhysRevB.99.140501) (2019).
23. Hohenberg, P. & Kohn, W. Inhomogeneous Electron Gas. *Phys. Rev.* **136**, B864–B871, DOI: [10.1103/PhysRev.136.B864](https://doi.org/10.1103/PhysRev.136.B864) (1964).
24. Kohn, W. & Sham, L. J. Self-Consistent Equations Including Exchange and Correlation Effects. *Phys. Rev.* **140**, A1133–A1138, DOI: [10.1103/PhysRev.140.A1133](https://doi.org/10.1103/PhysRev.140.A1133) (1965).
25. Anisimov, V. I. *et al.* Full orbital calculation scheme for materials with strongly correlated electrons. *Phys. Rev. B* **71**, 125119, DOI: [10.1103/PhysRevB.71.125119](https://doi.org/10.1103/PhysRevB.71.125119) (2005).
26. Kotliar, G. *et al.* Electronic structure calculations with dynamical mean-field theory. *Rev. Mod. Phys.* **78**, 865–951, DOI: [10.1103/RevModPhys.78.865](https://doi.org/10.1103/RevModPhys.78.865) (2006).

27. Lechermann, F. *et al.* Dynamical mean-field theory using Wannier functions: A flexible route to electronic structure calculations of strongly correlated materials. *Phys. Rev. B* **74**, 125120, DOI: [10.1103/PhysRevB.74.125120](https://doi.org/10.1103/PhysRevB.74.125120) (2006).
28. Prourovskii, L. V., Amadon, B., Biermann, S. & Georges, A. Self-consistency over the charge density in dynamical mean-field theory: A linear muffin-tin implementation and some physical implications. *Phys. Rev. B* **76**, 235101, DOI: [10.1103/PhysRevB.76.235101](https://doi.org/10.1103/PhysRevB.76.235101) (2007).
29. Amadon, B. *et al.* Plane-wave based electronic structure calculations for correlated materials using dynamical mean-field theory and projected local orbitals. *Phys. Rev. B* **77**, 205112, DOI: [10.1103/PhysRevB.77.205112](https://doi.org/10.1103/PhysRevB.77.205112) (2008).
30. Korotin, D. *et al.* Construction and solution of a Wannier-functions based Hamiltonian in the pseudopotential plane-wave framework for strongly correlated materials. *Eur. Phys. J. B* **65**, 91–98, DOI: [10.1140/epjb/e2008-00326-3](https://doi.org/10.1140/epjb/e2008-00326-3) (2008).
31. Haule, K., Yee, C.-H. & Kim, K. Dynamical mean-field theory within the full-potential methods: Electronic structure of CeIrIn<sub>5</sub>, CeCoIn<sub>5</sub>, and CeRhIn<sub>5</sub>. *Phys. Rev. B* **81**, 195107, DOI: [10.1103/PhysRevB.81.195107](https://doi.org/10.1103/PhysRevB.81.195107) (2010).
32. Haule, K. & Birol, T. Free energy from stationary implementation of the DFT + DMFT functional. *Phys. Rev. Lett.* **115**, 256402, DOI: [10.1103/PhysRevLett.115.256402](https://doi.org/10.1103/PhysRevLett.115.256402) (2015).
33. Plekhanov, E. *et al.* Many-body renormalization of forces in *f*-electron materials. *Phys. Rev. B* **98**, 075129, DOI: [10.1103/PhysRevB.98.075129](https://doi.org/10.1103/PhysRevB.98.075129) (2018).
34. Koskenmaki, D. C. & Gschneidner Jr, K. A. Cerium. *Handb. Phys. Chem. Rare Earths* **1**, 337–377, DOI: [10.1016/S0168-1273\(78\)01008-9](https://doi.org/10.1016/S0168-1273(78)01008-9) (1978).
35. Held, K., McMahan, A. K. & Scalettar, R. T. Cerium Volume Collapse: Results from the Merger of Dynamical Mean-Field Theory and Local Density Approximation. *Phys. Rev. Lett.* **87**, 276404, DOI: [10.1103/PhysRevLett.87.276404](https://doi.org/10.1103/PhysRevLett.87.276404) (2001).
36. Amadon, B., Biermann, S., Georges, A. & Aryasetiawan, F. The  $\alpha$ – $\gamma$  transition of cerium is entropy driven. *Phys. Rev. Lett.* **96**, 066402, DOI: [10.1103/PhysRevLett.96.066402](https://doi.org/10.1103/PhysRevLett.96.066402) (2006).
37. Haule, K. Quantum Monte Carlo impurity solver for cluster dynamical mean-field theory and electronic structure calculations with adjustable cluster base. *Phys. Rev. B* **75**, 155113, DOI: [10.1103/PhysRevB.75.155113](https://doi.org/10.1103/PhysRevB.75.155113) (2007).
38. Huang, L. & Lu, H. Electronic structure of cerium: A comprehensive first-principles study. *Phys. Rev. B* **99**, 045122, DOI: [10.1103/PhysRevB.99.045122](https://doi.org/10.1103/PhysRevB.99.045122) (2019).
39. Allen, J. *et al.* Electronic structure of cerium and light rare-earth intermetallics. *Adv. Phys.* **35**, 275–316, DOI: [10.1080/00018738600101901](https://doi.org/10.1080/00018738600101901) (1986).
40. Matar, S. F. Review on cerium intermetallic compounds: A bird’s eye outlook through DFT. *Prog. Solid State Chem.* **41**, 55–85, DOI: <https://doi.org/10.1016/j.progsolidstchem.2013.03.001> (2013).
41. McMahan, A. K., Huscroft, C., Scalettar, R. T. & Pollock, E. L. Volume-collapse transitions in the rare earth metals. *J. Comput. Mater. Des.* **5**, 131–162, DOI: [10.1023/A:1008698422183](https://doi.org/10.1023/A:1008698422183) (1998).
42. Söderlind, P., Turchi, P. E. A., Landa, A. & Lordi, V. Ground-state properties of rare-earth metals: an evaluation of density-functional theory. *J. Phys.: Cond. Matter* **26**, 416001, DOI: [10.1088/0953-8984/26/41/416001](https://doi.org/10.1088/0953-8984/26/41/416001) (2014).
43. Riseborough, P. S. Heavy fermion semiconductors. *Adv. Phys.* **49**, 257–320, DOI: [10.1080/000187300243345](https://doi.org/10.1080/000187300243345) (2000).
44. Tomczak, J. M. Thermoelectricity in correlated narrow-gap semiconductors. *J. Phys.: Condens. Matter* **30**, 183001, DOI: [10.1088/1361-648X/aab284](https://doi.org/10.1088/1361-648X/aab284) (2018).
45. Brüning, E. M. *et al.* Cefepo: A heavy fermion metal with ferromagnetic correlations. *Phys. Rev. Lett.* **101**, 117206, DOI: [10.1103/PhysRevLett.101.117206](https://doi.org/10.1103/PhysRevLett.101.117206) (2008).
46. Ohishi, K. *et al.* Development of the heavy-fermion state in Ce<sub>2</sub>IrIn<sub>8</sub> and the effects of Ce dilution in (Ce<sub>1-x</sub>La<sub>x</sub>)<sub>2</sub>IrIn<sub>8</sub>. *Phys. Rev. B* **80**, 125104, DOI: [10.1103/PhysRevB.80.125104](https://doi.org/10.1103/PhysRevB.80.125104) (2009).
47. Wang, C. *et al.* Effect of hole doping on superconductivity in compressed CeH<sub>9</sub> at high pressures. *Phys. Rev. B* **104**, L020504, DOI: [10.1103/PhysRevB.104.L020504](https://doi.org/10.1103/PhysRevB.104.L020504) (2021).
48. Jeon, H., Wang, C., Yi, S. & Cho, J.-H. Origin of enhanced chemical precompression in cerium hydride CeH<sub>9</sub>. *Sci. Rep.* **10**, 16878, DOI: [10.1038/s41598-020-73665-1](https://doi.org/10.1038/s41598-020-73665-1) (2020).
49. Parlinski, K., Li, Z. Q. & Kawazoe, Y. First-principles determination of the soft mode in cubic ZrO<sub>2</sub>. *Phys. Rev. Lett.* **78**, 4063–4066, DOI: [10.1103/PhysRevLett.78.4063](https://doi.org/10.1103/PhysRevLett.78.4063) (1997).
50. Monserrat, B. Electron–phonon coupling from finite differences. *J. Condens. Matter Phys.* **30**, 083001, DOI: [10.1088/1361-648X/aaa737](https://doi.org/10.1088/1361-648X/aaa737) (2018).
51. Koçer, C. P., Haule, K., Pascut, G. L. & Monserrat, B. Efficient lattice dynamics calculations for correlated materials with DFT + DMFT. *Phys. Rev. B* **102**, 245104, DOI: [10.1103/PhysRevB.102.245104](https://doi.org/10.1103/PhysRevB.102.245104) (2020).



52. Errea, I. *et al.* Quantum crystal structure in the 250-kelvin superconducting lanthanum hydride. *Nature* **578**, 66–69, DOI: [10.1038/s41586-020-1955-z](https://doi.org/10.1038/s41586-020-1955-z) (2020).
53. Khanal, G. & Haule, K. Correlation driven phonon anomalies in bulk FeSe. *Phys. Rev. B* **102**, 241108, DOI: [10.1103/PhysRevB.102.241108](https://doi.org/10.1103/PhysRevB.102.241108) (2020).
54. McMillan, W. L. Transition temperature of strong-coupled superconductors. *Phys. Rev.* **167**, 331–344, DOI: [10.1103/PhysRev.167.331](https://doi.org/10.1103/PhysRev.167.331) (1968).
55. Allen, P. B. & Dynes, R. C. Transition temperature of strong-coupled superconductors reanalyzed. *Phys. Rev. B* **12**, 905–922, DOI: [10.1103/PhysRevB.12.905](https://doi.org/10.1103/PhysRevB.12.905) (1975).
56. Morel, P. & Anderson, P. W. Calculation of the superconducting state parameters with retarded electron-phonon interaction. *Phys. Rev.* **125**, 1263–1271, DOI: [10.1103/PhysRev.125.1263](https://doi.org/10.1103/PhysRev.125.1263) (1962).
57. Allen, P. B. & Mitrović, B. Theory of superconducting  $T_c$ . *Solid State Phys.* **37**, 1–92, DOI: [10.1016/S0081-1947\(08\)60665-7](https://doi.org/10.1016/S0081-1947(08)60665-7) (1983).
58. Margine, E. R. & Giustino, F. Anisotropic Migdal-Eliashberg theory using Wannier functions. *Phys. Rev. B* **87**, 024505, DOI: [10.1103/PhysRevB.87.024505](https://doi.org/10.1103/PhysRevB.87.024505) (2013).
59. Plekhanov, E. *et al.* Computational materials discovery for lanthanide hydrides at high pressure for high temperature superconductivity. *Phys. Rev. Res.* **4**, 013248, DOI: [10.1103/PhysRevResearch.4.013248](https://doi.org/10.1103/PhysRevResearch.4.013248) (2022).
60. Hubbard, J. & Flowers, B. H. Electron correlations in narrow energy bands. *Proc. R. Soc. London, Ser. A* **276**, 238–257, DOI: [10.1098/rspa.1963.0204](https://doi.org/10.1098/rspa.1963.0204) (1963).
61. Gull, E. *et al.* Continuous-time monte carlo methods for quantum impurity models. *Rev. Mod. Phys.* **83**, 349–404, DOI: [10.1103/RevModPhys.83.349](https://doi.org/10.1103/RevModPhys.83.349) (2011).
62. Bardeen, J., Cooper, L. N. & Schrieffer, J. R. Theory of superconductivity. *Phys. Rev.* **108**, 1175–1204, DOI: [10.1103/PhysRev.108.1175](https://doi.org/10.1103/PhysRev.108.1175) (1957).
63. Tomczak, J. M. & Biermann, S. Effective band structure of correlated materials: the case of  $\text{VO}_2$ . *J. Phys.:Condens. Matter* **19**, 365206, DOI: [10.1088/0953-8984/19/36/365206](https://doi.org/10.1088/0953-8984/19/36/365206) (2007).
64. Yuan, Z. *et al.* Correlation-enhanced electron-phonon coupling and superconductivity in  $(\text{Ba},\text{K})\text{SbO}_3$  superconductors. *Phys. Rev. B* **105**, 014517, DOI: [10.1103/PhysRevB.105.014517](https://doi.org/10.1103/PhysRevB.105.014517) (2022).
65. Yin, Z. P., Kutepov, A. & Kotliar, G. Correlation-Enhanced Electron-Phonon Coupling: Applications of  $\text{GW}$  and Screened Hybrid Functional to Bismuthates, Chloronitrides, and Other High- $T_c$  superconductors. *Phys. Rev. X* **3**, 021011, DOI: [10.1103/PhysRevX.3.021011](https://doi.org/10.1103/PhysRevX.3.021011) (2013).
66. Blaha, P. *et al.* WIEN2k: An APW+lo program for calculating the properties of solids. *J. Chem. Phys.* **152**, 074101, DOI: [10.1063/1.5143061](https://doi.org/10.1063/1.5143061) (2020).
67. Kaufmann, J. & Held, K. Ana.cont: Python package for analytic continuation. *Comput. Phys. Commun.* **282**, 108519, DOI: [10.1016/j.cpc.2022.108519](https://doi.org/10.1016/j.cpc.2022.108519) (2023).
68. Segall, M. D. *et al.* First-principles simulation: Ideas, illustrations and the CASTEP code. *J. Phys. Condens.* **14**, 2717–2744, DOI: [10.1088/0953-8984/14/11/301](https://doi.org/10.1088/0953-8984/14/11/301) (2002).
69. Clark, S. J. *et al.* First principles methods using CASTEP. *Z. Kristallogr. Cryst. Mater.* **220**, 567–570, DOI: [10.1524/zkri.220.5.567.65075](https://doi.org/10.1524/zkri.220.5.567.65075) (2005).
70. Giannozzi, P. *et al.* QUANTUM ESPRESSO: A modular and open-source software project for quantum simulations of materials. *J. Phys. Condens.* **21**, 395502, DOI: [10.1088/0953-8984/21/39/395502](https://doi.org/10.1088/0953-8984/21/39/395502) (2009).
71. Giannozzi, P. *et al.* Advanced capabilities for materials modelling with Quantum ESPRESSO. *J. Phys.:Condens. Matter* **29**, 465901, DOI: [10.1088/1361-648X/aa8f79](https://doi.org/10.1088/1361-648X/aa8f79) (2017).
72. Perdew, J. P., Burke, K. & Ernzerhof, M. Generalized Gradient Approximation Made Simple. *Phys. Rev. Lett.* **77**, 3865–3868, DOI: [10.1103/PhysRevLett.77.3865](https://doi.org/10.1103/PhysRevLett.77.3865) (1996).
73. Tomczak, J. M., Miyake, T., Sakuma, R. & Aryasetiawan, F. Effective Coulomb interactions in solids under pressure. *Phys. Rev. B* **79**, 235133, DOI: [10.1103/PhysRevB.79.235133](https://doi.org/10.1103/PhysRevB.79.235133) (2009).
74. Abramovitch, D. J., Zhou, J.-J., Mravlje, J., Georges, A. & Bernardi, M. Combining electron-phonon and dynamical mean-field theory calculations of correlated materials: Transport in the correlated metal  $\text{Sr}_2\text{RuO}_4$ . *Phys. Rev. Mater.* **7**, 093801, DOI: [10.1103/PhysRevMaterials.7.093801](https://doi.org/10.1103/PhysRevMaterials.7.093801) (2023).
75. Abramovitch, D. J., Coulter, J., Beck, S. & Millis, A. Electron-phonon coupling in correlated metals: A dynamical mean-field theory study (2025).
76. Lloyd-Williams, J. H. & Monserrat, B. Lattice dynamics and electron-phonon coupling calculations using non-diagonal supercells. *Phys. Rev. B* **92**, 184301, DOI: [10.1103/PhysRevB.92.184301](https://doi.org/10.1103/PhysRevB.92.184301) (2015).
77. Poncé, S., Margine, E., Verdi, C. & Giustino, F. EPW: Electron-phonon coupling, transport and superconducting properties using maximally localized Wannier functions. *Comput. Phys. Commun.* **209**, 116–133, DOI: [10.1016/j.cpc.2016.07.028](https://doi.org/10.1016/j.cpc.2016.07.028) (2016).

78. Lee, H. *et al.* Electron–phonon physics from first principles using the EPW code. *npj Comput. Mater.* **9**, 156, DOI: [10.1038/s41524-023-01107-3](https://doi.org/10.1038/s41524-023-01107-3) (2023).

## Acknowledgements

The authors would like to thank C. Weber and E. Plekhanov for useful discussions. S.C. and B.M. acknowledge support from EPSRC [EP/V062654/1]. S.C. also acknowledges financial support from the Cambridge Trust and the Winton Program for the Physics of Sustainability. Y.W. acknowledges funding from the China Scholarship Council. B.M. also acknowledges support from a UKRI Future Leaders Fellowship [MR/V023926/1] and from the Gianna Angelopoulos Programme for Science, Technology, and Innovation. S.P. is a Research Associate of the Fonds de la Recherche Scientifique - FNRS. This publication was supported by the

Walloon Region in the strategic ax FRFS-WEL-T. Computational resources were provided through our membership in the UK's HEC Materials Chemistry Consortium, funded by EPSRC (EP/R029431 and EP/X035859). This work used ARCHER2, the UK National Supercomputing Service (<http://www.archer2.ac.uk>), as well as resources from the UK Materials and Molecular Modeling Hub (MMM Hub), which is partially supported by EPSRC (EP/T022213 and EP/W032260). Computational resources were also provided by the EuroHPC JU award granting access to MareNostrum5 at the Barcelona Supercomputing Center (BSC), Spain (Project ID: EHPC-EXT-2023E02-050), by the Consortium des Équipements de Calcul Intensif (CÉCI), funded by the FRS-FNRS under Grant No. 2.5020.11, by the Tier-1 supercomputer of the Walloon Region (Lucia) with infrastructure funded by the Walloon Region under the grant agreement n°1910247.

# Supplemental Information for Impact of strong correlation on the superconductivity of the high-pressure rare-earth CeH<sub>9</sub>

Siyu Chen,<sup>1,2</sup> Yao Wei,<sup>3</sup> Bartomeu Monserrat,<sup>1,2</sup> Jan Tomczak,<sup>3,4</sup> and Samuel Poncé<sup>5,6</sup>

<sup>1</sup>*TCM Group, Cavendish Laboratory, University of Cambridge,  
J. J. Thomson Avenue, Cambridge CB3 0HE, United Kingdom*

<sup>2</sup>*Department of Materials Science and Metallurgy, University of Cambridge,  
27 Charles Babbage Road, Cambridge CB3 0FS, United Kingdom*

<sup>3</sup>*Department of Physics, King's College London, Strand, London WC2R 2LS, United Kingdom*

<sup>4</sup>*Institute of Solid State Physics, TU Wien, 1040 Vienna, Austria*

<sup>5</sup>*European Theoretical Spectroscopy Facility, Institute of Condensed Matter and Nanosciences,  
Université catholique de Louvain, Chemin des Étoiles 8, B-1348 Louvain-la-Neuve, Belgium*

<sup>6</sup>*WEL Research Institute, avenue Pasteur 6, 1300 Wavre, Belgium*

## SECTION I: CRYSTAL STRUCTURE OF HIGH-PRESSURE CeH<sub>9</sub>

The high-pressure phase of CeH<sub>9</sub> was first theoretically predicted [1]. Subsequent experimental studies have confirmed its thermodynamic and stoichiometric stability under external pressure exceeding 80 GPa [2, 3]. The structure is shown in Fig. S1 crystallises in the space group P6<sub>3</sub>/mmc, where the cerium atoms form a hexagonal close-packed lattice. Each cerium atom is surrounded by 29 hydrogen atoms, and these hydrogen atoms can be considered as an octadecahedronal cage composed of six tetragonal rings, six pentagonal rings and six hexagonal rings. The rings share edges between contiguous octadecahedronal cages, giving rise to an extensive 3D hydrogen network structure. It is this special clathrate structure that allows high hydrogen content without the formation of H<sub>2</sub> molecules.

There are three chemically non-equivalent hydrogen sites in CeH<sub>9</sub> (highlighted in red, green and blue in Fig. S1), thereby the hydrogen atoms have four nearest-neighbour distances. Table S1 reports for the structural parameters of the hydrogen cage under the pressure of 200 GPa. Among them, we find that the ‘red’ and ‘green’ hydrogen atoms exhibit the shortest distance of 1.122 Å. This distance is comparable to that in metallic hydrogen at 500 GPa [4]. In this sense, cerium provides a chemical precompression pressure of nearly 300 GPa.

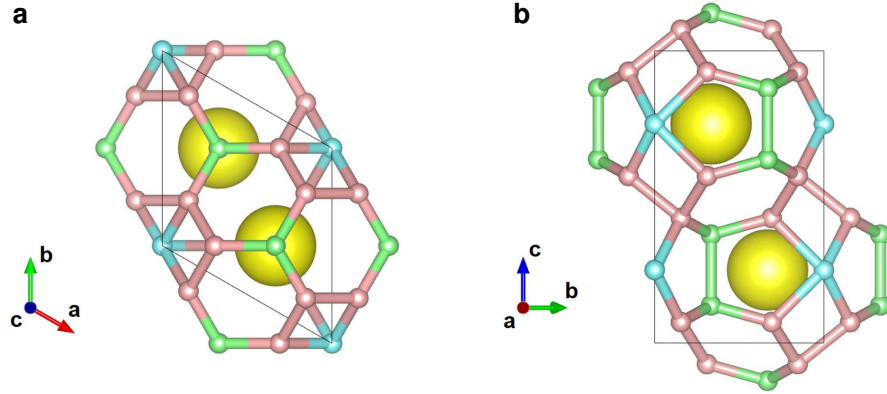


FIG. S1: (a) Top and (b) side views of the crystal structure of CeH<sub>9</sub>, where the cerium atom is inside the cage formed by hydrogen atoms. The hydrogen atoms with different chemical environments are distinguished in red, green and blue.

Compound	Space Group	Lattice Parameters	Atomic Sites	$x$	$y$	$z$	Nearest-neighbor distances
CeH <sub>9</sub>	P6 <sub>3</sub> /mmc	$a = 3.493 \text{ Å}$ $c = 5.230 \text{ Å}$	Ce	0.6667	0.3333	0.2500	H <sub>r</sub> -H <sub>r</sub> = 1.200 Å
			H <sub>r</sub>	0.1546	0.8454	0.4282	H <sub>r</sub> -H <sub>g</sub> = 1.122 Å
			H <sub>g</sub>	0.3333	0.6667	0.1291	H <sub>r</sub> -H <sub>b</sub> = 1.320 Å
			H <sub>b</sub>	0.0000	0.0000	0.7500	H <sub>g</sub> -H <sub>g</sub> = 1.264 Å

TABLE S1: Lattice parameters and atomic positions for the CeH<sub>9</sub> crystallizing in the P6<sub>3</sub>/mmc space group, including lattice parameters, atomic sites, fractional coordinates ( $x$ ,  $y$ ,  $z$ ), and nearest-neighbor distances.

## SECTION II: DENSITY OF STATES AND SPECTRAL FUNCTIONS

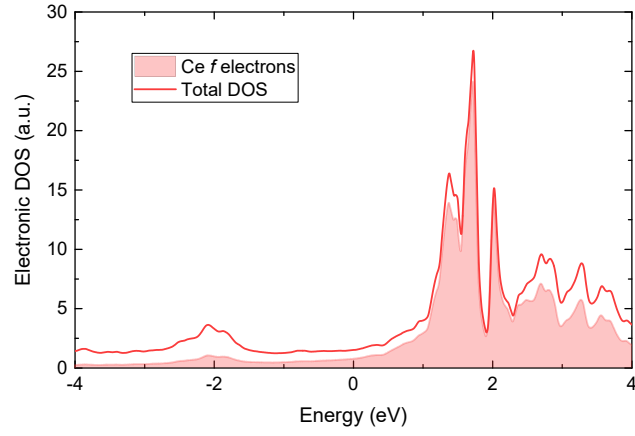


FIG. S2: Density of states (DOS) of  $\text{CeH}_9$  calculated through DFT, where the contribution of cerium  $f$ -electrons is highlighted.

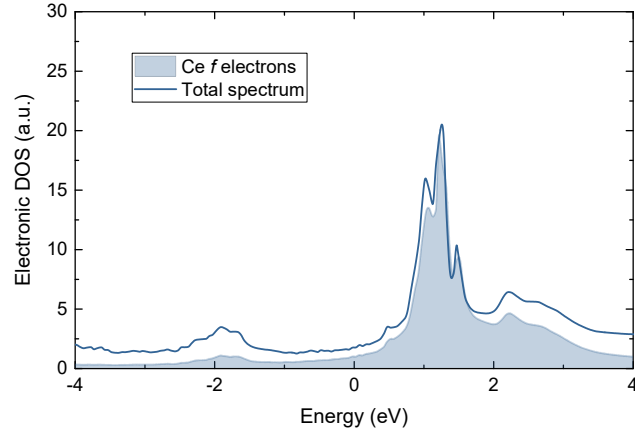


FIG. S3: Spectral function of  $\text{CeH}_9$  calculated through DFT+DMFT, where the contribution of cerium  $f$ -electrons is highlighted.

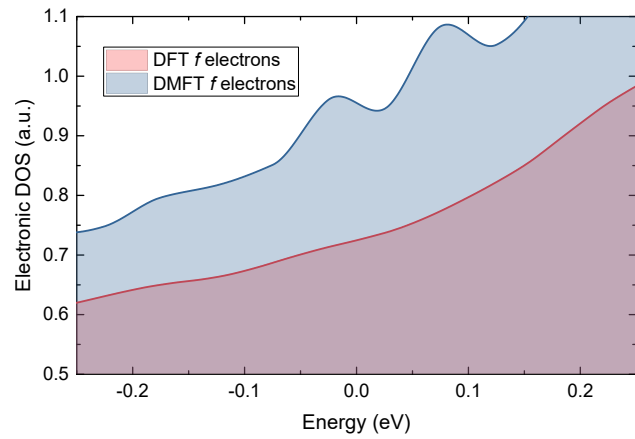


FIG. S4: Contribution of cerium  $f$ -electrons to the density of states (DOS) and total spectral function calculated through DFT (red) DFT+DMFT (blue), respectively.



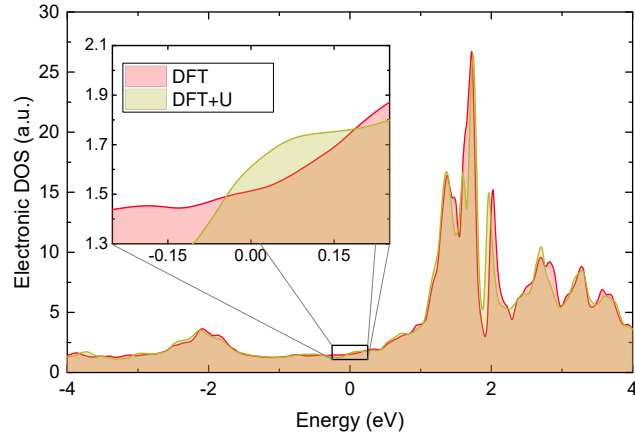


FIG. S5: Density of states (DOS) of  $\text{CeH}_9$  calculated through DFT (red) and DFT+U (yellow).

### SECTION III: SELF-ENERGY

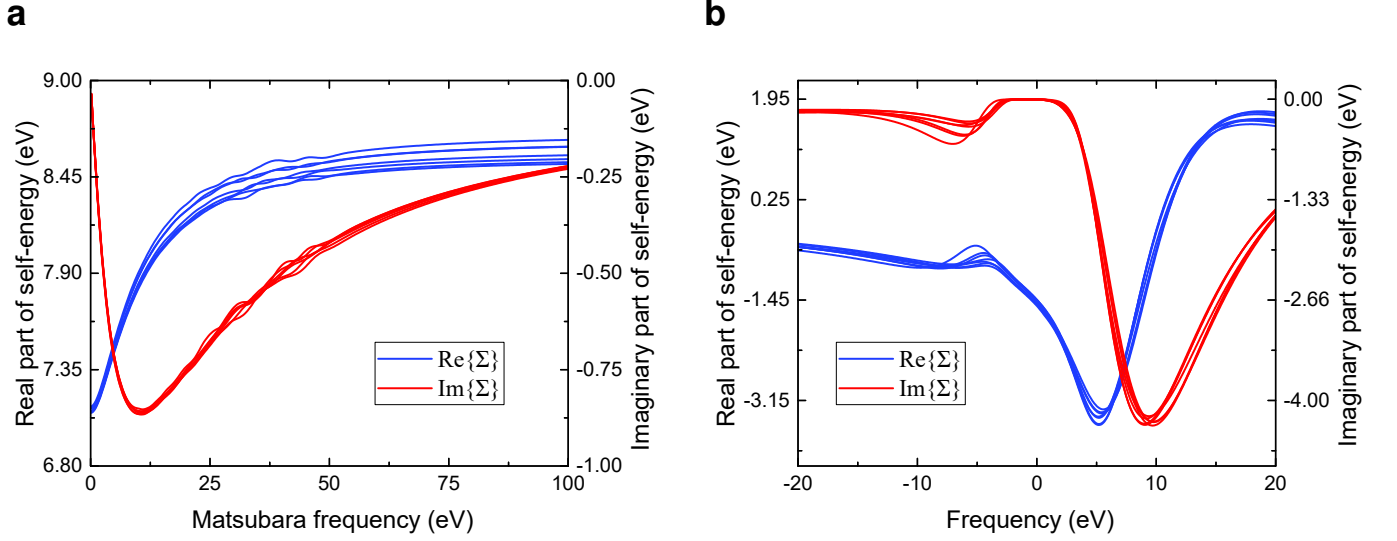


FIG. S6: Real and imaginary parts of the diagonal terms of the electronic self-energy operator in the basis of seven  $4f$ -orbitals, shown as functions along **a** the imaginary frequency axis and **b** the real frequency axis.

## SECTION IV: COMPARISON OF DFT AND DMFT-RENORMALIZED BAND STRUCTURES

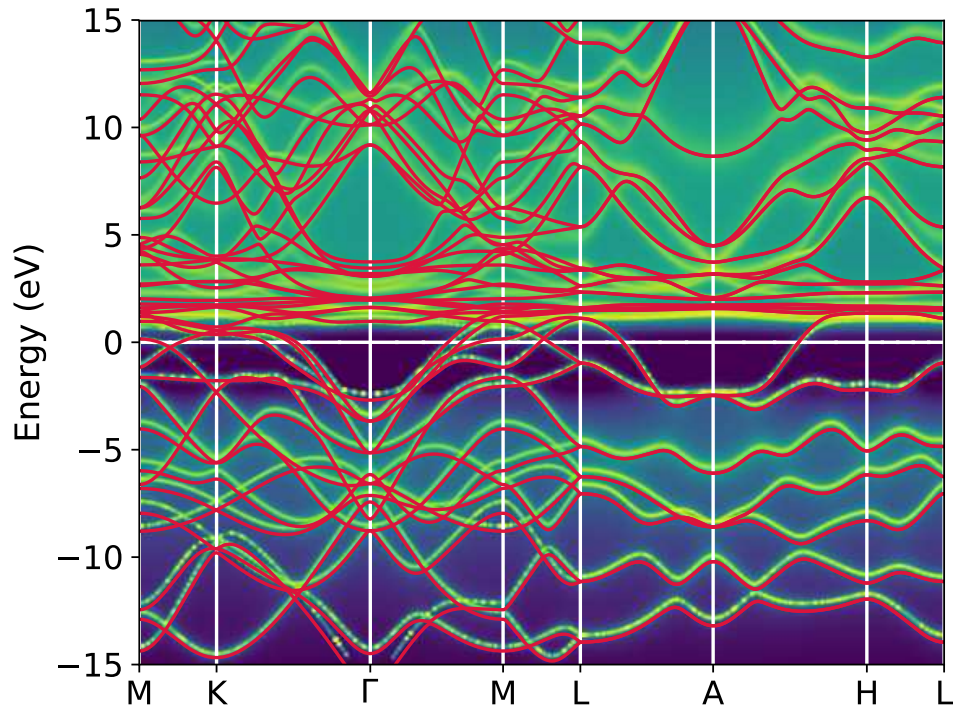


FIG. S7: Momentum-resolved spectral function  $A_{\mathbf{k}}(\omega)$  of  $\text{CeH}_9$  along a high-symmetry path calculated with DFT+DMFT (color map) compared to the DFT bands.

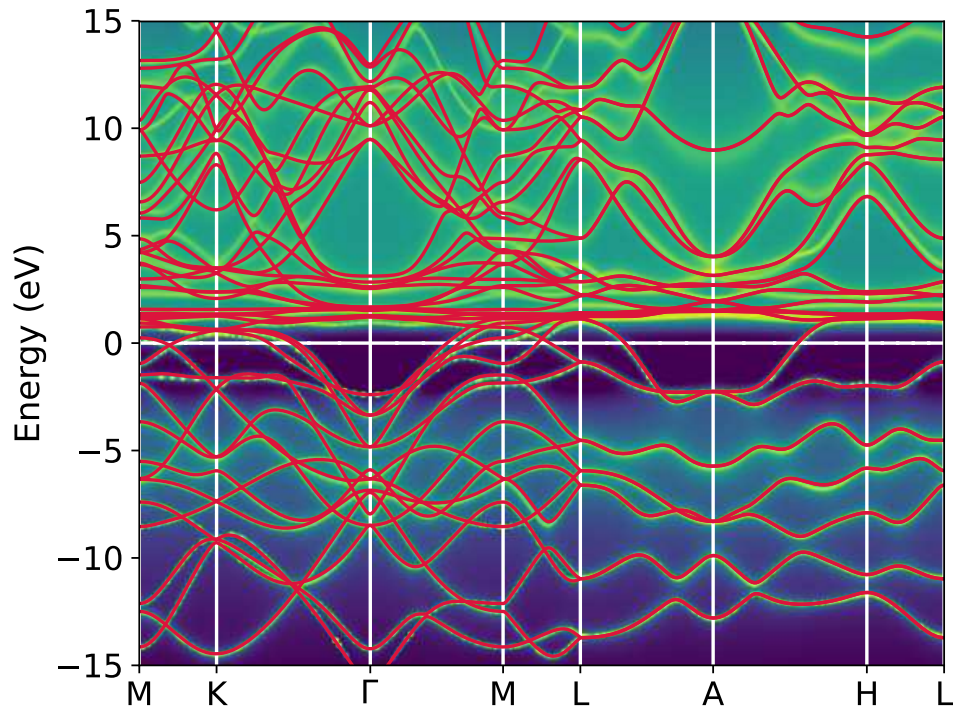


FIG. S8: Momentum-resolved spectral function  $A_{\mathbf{k}}(\omega)$  of  $\text{CeH}_9$  along a high-symmetry path calculated with DFT+DMFT (color map) compared to the DMFT-renormalized bands.

## SECTION V: DFT+DMFT

Dynamical mean field theory (DMFT) was initially developed to address the Hubbard model, a fundamental model for studying strongly correlated electron systems. Shortly after its inception, DMFT was integrated with density functional theory (DFT), giving rise to the first-principles method known as DFT+DMFT. This approach has achieved significant success, particularly in accurately predicting the electronic structures of Mott insulators and correlated metals. Here we briefly present technical details.

There currently exist several computational schemes for integrating DFT and DMFT [5–13], each with its pros and cons. We adopt the latest scheme proposed in Refs. [12, 13], which connects DFT and DMFT by the down- and up-folding (also known as projection and embedding) operations. Specifically, the whole orbital space of electrons is partitioned into two: Bloch orbitals space  $\mathbb{V}\{|\varphi_{n\mathbf{k}}\rangle\}$  for the DFT self-consistent loop of electron density and correlated local orbital space  $\mathbb{V}\{|\vartheta_i\rangle\}$  for the DMFT self-consistent loop of the Green function. The calculation proceeds as follows: (i) From the Kohn-Sham eigenstates, one obtains the Kohn-Sham Green function  $G_{n\mathbf{k}}^{\text{KS}}(\omega)$  and then down-fold it into  $\mathbb{V}\{|\vartheta_i\rangle\}$ . (ii) Using the down-folded Green function as the input, the Anderson impurity model solver generates the impurity Green function  $G_i^{\text{AI}}(\omega)$ . (iii) From  $G_i^{\text{AI}}(\omega)$ , one extracts the self-energy  $\Sigma(\omega)$  and then up-folding it into  $\mathbb{V}\{|\varphi_{n\mathbf{k}}\rangle\}$ . (iv) With the up-folded self-energy, the Dyson equation is solved for the lattice Green function. (v) The lattice Green function is fed back into the DFT loop, allowing the update of the electron density and construction of the Kohn-Sham Hamiltonian. (vi) Solving the Kohn-Sham Hamiltonian yields a new set of Kohn-Sham eigenstates, after which one returns to step (i) and iterates until the whole loop reaches self-consistency.

In addition, the above scheme is featured by defining a DFT+DMFT energy functional whose form can be simply summarised as follows

$$\Gamma[n(\mathbf{r}), G^{\text{AI}}(\omega)] = T_{\text{el}}[n(\mathbf{r}), G^{\text{AI}}(\omega)] + \int d\mathbf{r} [V_{\text{el-nu}}(\mathbf{r}) + V_{\text{H}}(\mathbf{r})] n(\mathbf{r}) + E_{\text{XC}}[n(\mathbf{r}), G^{\text{AI}}(\omega)]. \quad (\text{S1})$$

Here the electrostatic potential  $V_{\text{el-nu}}(\mathbf{r})$  arising from nuclei and the Hartree potential  $V_{\text{H}}(\mathbf{r})$  are the same as they are in DFT. However, the kinetic energy functional  $T_{\text{el}}[n(\mathbf{r}), G^{\text{AI}}(\omega)]$  and the exchange-correlation functional  $E_{\text{XC}}[n(\mathbf{r}), G^{\text{AI}}(\omega)]$  exhibit a greater degree of sophistication than those in DFT, i.e. they depend not only on the ground-state electron density  $n(\mathbf{r})$  of the Kohn-Sham system that the material of interest is mapped to, but also on the impurity Green function  $G^{\text{AI}}(\omega)$  of the corresponding Anderson impurity model. Notably, the energy functional  $\Gamma[n(\mathbf{r}), G^{\text{AI}}(\omega)]$  can be recast into the form of the well-known Baym-Kadanoff functional [6, 14], from which the physical meaning of  $\Gamma[n(\mathbf{r}), G^{\text{AI}}(\omega)]$  can be further revealed as the free energy of the system. It is worth noting that this functional is stationary, i.e. the variation of this functional with respect to the electron Green function always vanishes. This means that any (first order) perturbation in the electron Green function can lead to only a minor (second order) variation in the free energy, and it follows that the corresponding numerical calculations involving energy and force can be implemented robustly. This crucial feature empowers us not only to calculate spectroscopic quantities of the system, but also to conduct geometry optimisation and force calculations at the DFT+DMFT level.

## SECTION VI: COMPARISON OF PSEUDOPOTENTIAL-DFT AND ALL-ELECTRON-DFT

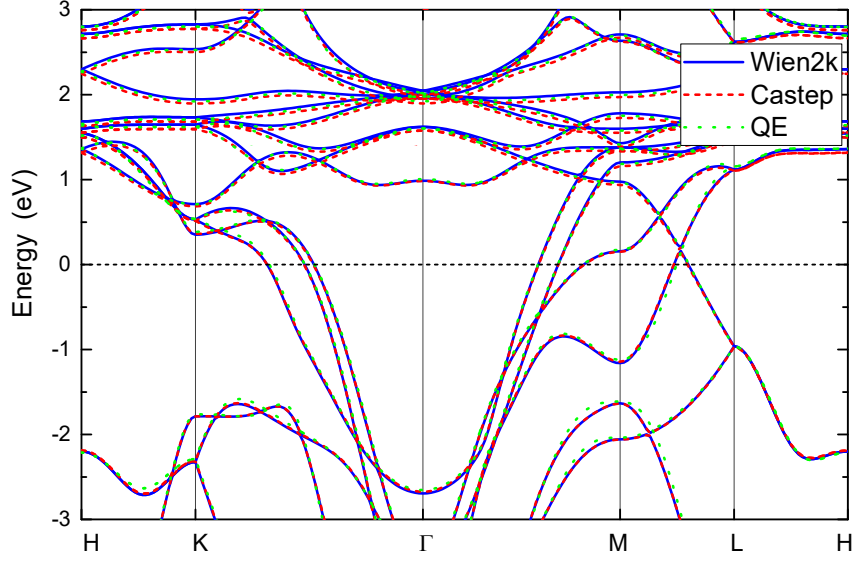


FIG. S9: Comparison of band structures calculated by WIEN2k using the all-electron method and by CASTEP and QUANTUM ESPRESSO (QE) using the pseudopotential method.

## SECTION VII: ELIASHBERG THEORY OF SUPERCONDUCTIVITY

For completeness, here we present Eliashberg theory of superconductivity. We start directly from the pairing self-energy found by the theory [15]:

$$\Sigma_{n\mathbf{k}}(i\omega_j) = i\omega_j [1 - \Upsilon_{n\mathbf{k}}(i\omega_j)] \mathbb{I} + \Lambda_{n\mathbf{k}}(i\omega_j) \sigma_x + \Xi_{n\mathbf{k}}(i\omega_j) \sigma_z. \quad (\text{S2})$$

Here  $\omega_j = (2j+1)\pi k_B T$  is the fermionic Matsubara frequency with  $j \in \mathbb{Z}$ , and the  $\sigma_y$  component is already dropped as it can always be suppressed to zero by performing a gauge transformation on  $\Lambda_{n\mathbf{k}}$ . This self-energy behaves as a  $2 \times 2$  matrix since the corresponding electron Green function is expressed in the Nambu-Gorkov formalism (so that electrons and Cooper pairs can be treated on the same footing). The non-diagonal component  $\Lambda_{n\mathbf{k}}$  becomes nonzero in the superconducting phase, which can be regarded as the superconducting order parameter, while the diagonal components  $\Upsilon_{n\mathbf{k}}$  and  $\Xi_{n\mathbf{k}}$  represent the renormalization of the electronic structure and the shift of the Fermi level respectively. This self-energy is expressed in terms of the electron Green function within the Migdal approximation [16] for the el-ph coupling contribution and the GW approximation [17] for the el-el interaction contribution. Substituting Eq.(S2) into the Dyson equation yields a set of self-consistent coupled equations:

$$\Upsilon_{n\mathbf{k}}(i\omega_j) = 1 + \frac{k_B T}{\omega_j N_F} \sum_{mj'\mathbf{k}'} \frac{\omega_{j'} \Upsilon_{m\mathbf{k}'}(i\omega_{j'})}{\theta_{m\mathbf{k}'}(i\omega_{j'})} \lambda_{n\mathbf{k}m\mathbf{k}'}(\omega_j - \omega_{j'}), \quad (\text{S3})$$

$$\Lambda_{n\mathbf{k}}(i\omega_j) = \frac{k_B T}{N_F} \sum_{mj'\mathbf{k}'} \frac{\Lambda_{m\mathbf{k}'}(i\omega_{j'})}{\theta_{m\mathbf{k}'}(i\omega_{j'})} [\lambda_{n\mathbf{k}m\mathbf{k}'}(\omega_j - \omega_{j'}) - N_F V_{n\mathbf{k}m\mathbf{k}'}], \quad (\text{S4})$$

$$\Xi_{n\mathbf{k}}(i\omega_j) = -\frac{k_B T}{N_F} \sum_{mj'\mathbf{k}'} \frac{E_{m\mathbf{k}'} - E_F + \Xi_{m\mathbf{k}'}(i\omega_{j'})}{\theta_{m\mathbf{k}'}(i\omega_{j'})} \lambda_{n\mathbf{k}m\mathbf{k}'}(\omega_j - \omega_{j'}), \quad (\text{S5})$$



where  $k_B$  is the Boltzmann constant,  $N_F$  is the density of states per spin at the Fermi level  $E_F$ ,  $V_{n\mathbf{k}m\mathbf{k}'}$  represents the matrix element of the el-el interaction, and  $\theta_{n\mathbf{k}}$  is an auxiliary quantity relating  $\Upsilon_{n\mathbf{k}}$ ,  $\Lambda_{n\mathbf{k}}$  and  $\Xi_{n\mathbf{k}}$  by

$$\theta_{n\mathbf{k}}(i\omega_j) = [\omega_j \Upsilon_{n\mathbf{k}}(i\omega_j)]^2 + [E_{n\mathbf{k}} - E_F + \Xi_{n\mathbf{k}}(i\omega_j)]^2 + [\Lambda_{n\mathbf{k}}(i\omega_j)]^2. \quad (\text{S6})$$

It is often that Eqs.(S3)-(S5) are supplemented by a particle number conservation condition so that  $E_F$  can be determined according to

$$N_e = \sum_{n\mathbf{k}} \left[ 1 - 2k_B T \sum_j \frac{E_{n\mathbf{k}} - E_F + \Xi_{n\mathbf{k}}(i\omega_j)}{\theta_{n\mathbf{k}}(i\omega_j)} \right], \quad (\text{S7})$$

where  $N_e$  is the number of electrons per unit cell. The quantity  $\lambda_{n\mathbf{k}m\mathbf{k}'}$ , which appears in all equations involving  $\Upsilon_{n\mathbf{k}}$ ,  $\Lambda_{n\mathbf{k}}$  and  $\Xi_{n\mathbf{k}}$ , characterizes the (anisotropic) el-ph coupling strength of the system, and it is given by

$$\lambda_{n\mathbf{k}m\mathbf{k}'}(\omega_j) = \int_0^\infty d\omega \alpha^2 F_{n\mathbf{k}m\mathbf{k}'}(\omega) \frac{2\omega}{\omega_j^2 + \omega^2}, \quad (\text{S8})$$

where

$$\alpha^2 F_{n\mathbf{k}m\mathbf{k}'}(\omega) = N_F \sum_\nu |g_{m\nu}(\mathbf{k}, \mathbf{q})|^2 \delta(\omega - \omega_{\nu\mathbf{q}}) \quad (\text{S9})$$

is referred to as the (anisotropic) *Eliashberg spectral function*. Here  $g_{m\nu}(\mathbf{k}, \mathbf{q}) = \langle \varphi_{m\mathbf{k}+\mathbf{q}} | \partial_{\nu\mathbf{q}} V | \varphi_{n\mathbf{k}} \rangle$  with  $\mathbf{q} = \mathbf{k}' - \mathbf{k}$  is known as the el-ph coupling matrix. In principle, once all the matrix elements of  $g_{m\nu}(\mathbf{k}, \mathbf{q})$  are known, together with the band structure  $E_{n\mathbf{k}}$  and the phonon dispersion  $\omega_{\nu\mathbf{q}}$ , one can solve Eqs.(S3)-(S5) self-consistently in a range of temperature. The highest temperature that leads to the non-trivial solution  $\Lambda_{n\mathbf{k}}(i\omega_j) \neq 0$  corresponds to the superconducting critical temperature.

A common simplification of Eqs.(S3)-(S5) is to only take into account el-ph scattering processes involving electrons with energies and momenta in the vicinity of the Fermi surface, i.e. restricting the energy concerned in Eqs.(S3)-(S5) to a relatively narrow window around the Fermi level. In this scheme, the density of states within the energy window is generally assumed to be a constant. It follows that within this approximation the Fermi level shift induced by  $\Xi_{n\mathbf{k}}$  vanishes and the particle number conservation condition is automatically satisfied. As a result, only two equations for  $\Upsilon_{n\mathbf{k}}$  and  $\Delta_{n\mathbf{k}}(i\omega_j) = \Lambda_{n\mathbf{k}}(i\omega_j) / \Upsilon_{n\mathbf{k}}(i\omega_j)$  need to be solved:

$$\Upsilon_{n\mathbf{k}}(i\omega_j) = 1 + \frac{\pi k_B T}{N_F \omega_j} \sum_{mj'\mathbf{k}'} \frac{\omega_{j'}}{\sqrt{\omega_{j'}^2 + \Delta_{m\mathbf{k}'}^2(i\omega_{j'})}} \lambda_{n\mathbf{k}m\mathbf{k}'}(\omega_j - \omega_{j'}) \delta(E_{m\mathbf{k}'} - E_F), \quad (\text{S10})$$

$$\Upsilon_{n\mathbf{k}}(i\omega_j) \Delta_{n\mathbf{k}}(i\omega_j) = \frac{\pi k_B T}{N_F} \sum_{mj'\mathbf{k}'} \frac{\Delta_{m\mathbf{k}'}(i\omega_{j'})}{\sqrt{\omega_{j'}^2 + \Delta_{m\mathbf{k}'}^2(i\omega_{j'})}} [\lambda_{n\mathbf{k}m\mathbf{k}'}(\omega_j - \omega_{j'}) - \mu_c] \delta(E_{m\mathbf{k}'} - E_F). \quad (\text{S11})$$

Equations (S10) and (S11) are referred to as the anisotropic Eliashberg equations, whose solution  $\Delta_{n\mathbf{k}}(i\omega_j)$  corresponds to the superconducting gap—a quantity that can be directly observed in experiments. Here we have replaced  $N_F V_{n\mathbf{k}m\mathbf{k}'}$  with the so-called Morel-Anderson pseudopotential  $\mu_c$ , which is a semi-empirical parameter describing the Coulomb repulsion of the system [18]. As with Eqs.(S10) and (S11), one can solve Eqs.(S10)-(S11) self-consistently in a proper range of temperature to determine  $T_c$ . In particular, when the anisotropy near the Fermi surface is negligible, Eqs.(S10)-(S11) can reduce to an isotropic form:

$$\Upsilon(i\omega_j) = 1 + \frac{\pi k_B T}{\omega_j} \sum_{j'} \frac{\omega_{j'}}{\sqrt{\omega_{j'}^2 + \Delta^2(i\omega_{j'})}} \lambda(\omega_j - \omega_{j'}), \quad (\text{S12})$$

$$\Upsilon(i\omega_j) \Delta(i\omega_j) = \pi k_B T \sum_{j'} \frac{\Delta(i\omega_{j'})}{\sqrt{\omega_{j'}^2 + \Delta^2(i\omega_{j'})}} [\lambda(\omega_j - \omega_{j'}) - \mu_c], \quad (\text{S13})$$

where  $\lambda(\omega_j)$  is referred to as the isotropic el-ph coupling strength and it can be obtained from Eq.(S8) as well, with the only difference being that  $\alpha^2 F_{n\mathbf{k}m\mathbf{k}'}(\omega)$  is replaced by its average over the Fermi surface:

$$\alpha^2 F(\omega) = \frac{1}{N_F} \sum_{\substack{\mathbf{k}\mathbf{q} \\ m\nu}} |g_{m\nu}(\mathbf{k}, \mathbf{q})|^2 \delta(\omega - \omega_{\nu\mathbf{q}}) \delta(E_{n\mathbf{k}} - E_F) \delta(E_{m\mathbf{k}+\mathbf{q}} - E_F). \quad (\text{S14})$$

The sum here includes the product of Dirac's delta functions  $\sum_{\substack{\mathbf{k}\mathbf{q} \\ m\nu}} \delta(E_{n\mathbf{k}} - E_F) \delta(E_{m\mathbf{k}+\mathbf{q}} - E_F)$ , which can be interpreted as that the el-ph coupling matrix is averaged over the Fermi surface.

In attempts to simplify the determination of superconducting transition temperature, McMillan [19] has introduced a semi-empirical equation describing the relationship between a simplified el-ph coupling strength and the critical temperature by fitting the theoretical solutions to isotropic Eliashberg equations of various metals. Following it, Allen and Dynes [20] further generalised the formula and obtained a direct expression of  $T_c$  as follows:

$$T_c = \frac{\omega_{\text{ln}}}{1.2k_B} \exp \left[ \frac{-1.04(1 + \lambda)}{\lambda - \mu_c(1 + 0.62\lambda)} \right]. \quad (\text{S15})$$

Equation (S15) is known as the McMillan-Allen-Dynes formula, where  $\omega_{\text{ln}}$  is the logarithmic average of phonon frequency given by

$$\omega_{\text{ln}} = \exp \left[ \frac{2}{\lambda} \int_0^\infty d\omega \frac{\alpha^2 F(\omega)}{\omega} \ln \omega \right]. \quad (\text{S16})$$

Additionally, the el-ph coupling strength appearing in Eq.(S15) has completely reduced to a number  $\lambda$  (from the function of  $\omega$ ), with a simpler definition compared to Eq.(S8) as follows:

$$\lambda = 2 \int_0^\infty d\omega \frac{\alpha^2 F(\omega)}{\omega}, \quad (\text{S17})$$

where  $\alpha^2 F(\omega)$  keeps the same form as that in Eq.(S14).

- 
- [1] F. Peng, Y. Sun, C. J. Pickard, R. J. Needs, Q. Wu, and Y. Ma, Phys. Rev. Lett. **119**, 107001 (2017), URL <https://link.aps.org/doi/10.1103/PhysRevLett.119.107001>.
  - [2] N. P. Salke, M. M. Davari Esfahani, Y. Zhang, I. A. Kruglov, J. Zhou, Y. Wang, E. Greenberg, V. B. Prakapenka, J. Liu, A. R. Oganov, et al., Nat. Commun. **10**, 4453 (2019), URL <https://doi.org/10.1038/s41467-019-12326-y>.
  - [3] X. Li, X. Huang, D. Duan, C. J. Pickard, D. Zhou, H. Xie, Q. Zhuang, Y. Huang, Q. Zhou, B. Liu, et al., Nat. Commun. **10**, 3461 (2019), URL <https://doi.org/10.1038/s41467-019-11330-6>.
  - [4] S. Azadi, B. Monserrat, W. M. C. Foulkes, and R. J. Needs, Phys. Rev. Lett. **112**, 165501 (2014), URL <https://link.aps.org/doi/10.1103/PhysRevLett.112.165501>.
  - [5] V. I. Anisimov, D. E. Kondakov, A. V. Kozhevnikov, I. A. Nekrasov, Z. V. Pchelkina, J. W. Allen, S.-K. Mo, H.-D. Kim, P. Metcalf, S. Suga, et al., Phys. Rev. B **71**, 125119 (2005), URL <https://link.aps.org/doi/10.1103/PhysRevB.71.125119>.
  - [6] G. Kotliar, S. Y. Savrasov, K. Haule, V. S. Oudovenko, O. Parcollet, and C. A. Marianetti, Rev. Mod. Phys. **78**, 865 (2006), URL <https://link.aps.org/doi/10.1103/RevModPhys.78.865>.
  - [7] F. Lechermann, A. Georges, A. Poteryaev, S. Biermann, M. Posternak, A. Yamasaki, and O. K. Andersen, Phys. Rev. B **74**, 125120 (2006), URL <https://link.aps.org/doi/10.1103/PhysRevB.74.125120>.
  - [8] L. V. Pourovskii, B. Amadon, S. Biermann, and A. Georges, Phys. Rev. B **76**, 235101 (2007), URL <https://link.aps.org/doi/10.1103/PhysRevB.76.235101>.
  - [9] B. Amadon, F. Lechermann, A. Georges, F. Jollet, T. O. Wehling, and A. I. Lichtenstein, Phys. Rev. B **77**, 205112 (2008), URL <https://link.aps.org/doi/10.1103/PhysRevB.77.205112>.
  - [10] D. Korotin, A. V. Kozhevnikov, S. L. Skornyakov, I. Leonov, N. Binggeli, V. I. Anisimov, and G. Trimarchi, Eur. Phys. J. B **65**, 91 (2008), URL <https://doi.org/10.1140/epjb/e2008-00326-3>.
  - [11] K. Haule, C.-H. Yee, and K. Kim, Phys. Rev. B **81**, 195107 (2010), URL <https://link.aps.org/doi/10.1103/PhysRevB.81.195107>.
  - [12] K. Haule and T. Birol, Phys. Rev. Lett. **115**, 256402 (2015), URL <https://link.aps.org/doi/10.1103/PhysRevLett.115.256402>.
  - [13] E. Plekhanov, P. Hasnip, V. Sacksteder, M. Probert, S. J. Clark, K. Refson, and C. Weber, Phys. Rev. B **98**, 075129 (2018), URL <https://link.aps.org/doi/10.1103/PhysRevB.98.075129>.
  - [14] G. Baym and L. P. Kadanoff, Phys. Rev. **124**, 287 (1961), URL <https://link.aps.org/doi/10.1103/PhysRev.124.287>.

- [15] P. B. Allen and B. Mitrović (Academic Press, 1983), vol. 37 of *Solid State Physics*, pp. 1–92, URL <https://www.sciencedirect.com/science/article/pii/S0081194708606657>.
- [16] A. B. Migdal, Sov. Phys. JETP **7**, 996 (1958).
- [17] L. Hedin, Phys. Rev. **139**, A796 (1965), URL <https://link.aps.org/doi/10.1103/PhysRev.139.A796>.
- [18] P. Morel and P. W. Anderson, Phys. Rev. **125**, 1263 (1962), URL <https://link.aps.org/doi/10.1103/PhysRev.125.1263>.
- [19] W. L. McMillan, Phys. Rev. **167**, 331 (1968), URL <https://link.aps.org/doi/10.1103/PhysRev.167.331>.
- [20] P. B. Allen and R. C. Dynes, Phys. Rev. B **12**, 905 (1975), URL <https://link.aps.org/doi/10.1103/PhysRevB.12.905>.